Science and Technology Indonesia
e-ISSN:2580-4391 *p*-ISSN:2580-4405
Vol. 11, No. 2, April 2026

Research Paper

Large SiO_2 Sizes Influencing Light Scattering Properties in Original White LED Structure

Pham Hong Cong[1], Nguyen Thi Phuong Loan[2*], Hsiao-Yi Lee[3]

[1]*Faculty of Electrical Engineering Technology, Industrial University of Ho Chi Minh City, Ho Chi Minh City, 70000, Vietnam*
[2]*Faculty of Fundamental 2, Posts and Telecommunications Institute of Technology, Ho Chi Minh City, 70000, Vietnam*
[3]*Department of Electrical Engineering, National Kaohsiung University of Science and Technology, Kaohsiung City, 807618, Taiwan*
*__Corresponding author__: ntploan@ptithcm.edu.vn

Abstract

Previously, SiO_2 particles (1-10 wt%, <10 μm) were proposed to augment the light flux and correlated color temperature (CCT) deviation in conventional blue-excited LEDs. This research paper explores the application of larger SiO_2 particle sizes within a conventional LED model. SiO_2 particles with diameters ranging from 1 μm to 20 μm were analyzed for their scattering properties using the Stober method, Mie-scattering-based MATLAB program and LightTools software to simulate optical attributes of a phosphor-transmuted WLED apparatus with XRD, SEM, and so on. SiO_2 was integrated into the yellow phosphor YAG:Ce layer to induce scattering phenomena within the active layer. Through our investigation, the concentrations of SiO_2 and YAG:Ce phosphor were consistently maintained at 5 and 10 wt.%, respectively. Our findings focus on assessing backward scattering with larger SiO_2 sizes. Modulating the sizes of SiO_2 spheres reduced CCT deviation and enhanced both flux output and color rendering performance. These results emphasize the potential utility of larger SiO_2 particles in enhancing white LED performance and facilitate further investigation to optimize their useability in production processes.

Keywords
Color Rendering, Mie Scattering, Luminous Flux, SiO_2

Received: 14 November 2025, Accepted: 18 February 2026
https://doi.org/10.26554/sti.2026.11.2.596-608

1. INTRODUCTION

The light-emitting diode (LED) plays an imperative role in promoting the efficiency of the solid-state illumination, and are applied to different fields, for example, sensing, biomedical detection and treatment, transportation, and display (Navarro et al., 2021; Yamashita et al., 2021; Suchkov et al., 2021). Advancements in LEDs' performance are, therefore, critical to the wide-spread development and application of multifunctional solid-state illuminating technology. The original LED was developed using the single blue chip to excite the yellow phosphor material YAG:Ce^{3+} (Zhou et al., 2021; Gao et al., 2021; Pi et al., 2021). The blending process between the transmitted blue light and phosphor-converted yellow light leads to light generation precepted as "white". However, the missing red emission in the total light wavelength and poor light scattering cause the light output to be cold and unevenly distributed on the target objects, resulting in low-rendering performance (Wang et al., 2021; Sun et al., 2021).

In addressing color deviation issues within LED lighting systems, the utilization of scattering phenomena to disperse light at wider angles has proven to be an effective strategy. Numerous methodologies have been proposed to regulate light scattering within LED packages, encompassing alterations to phosphor structures and the integration of scattering-inducing elements (Bugoffa and Chatterjee, 2021; Rahman et al., 2021; Chen et al., 2021; Li et al., 2021; Preciado et al., 2021). Among these elements, silicon dioxide (SiO_2) nanoparticles have garnered significant attention due to their exceptional scattering properties, emerging as favored agents for inducing scattering in optical systems, notably LEDs. SiO_2 was used to enhance the light flux and correlated color temperature (CCT) deviation of the white LED while reducing the concentration of YAG:Ce^{3+} to about 5-1 wt.% (Buzzelli and Erba, 2021). An earlier study also demonstrated using SiO_2 nano-bowl photonic crystal to improve the emission divergence angle and light transmission power of the conventional InGaN LEDs (Masaoka, 2021). Such reports successfully prove the potential of SiO_2 utilization in advanced white LED production. However, these papers discussed the varying concentration of SiO_2 but barely mentioned the material's particle sizes. Some studies mentioned the sizes of SiO_2, but the size was often less than 10 microns. Larger sizes of SiO_2 and how the varying radii impact the white LED performance has not been tested in detail. Other past studies have also considered examining SiO_2

alongside other potential phosphors (Loan and Anh, 2020c; Anh et al., 2025; Dang et al., 2021; Thi et al., 2021). However, these studies assess the particle size of SiO_2 in either a very small range or a much larger range without narrowing down to an optimal range that can be practical for many applications. The study herein aims to examine a smaller range of SiO_2 particle size that include optimal values for desirable scattering in WLED apparatuses.

In this research paper, larger sizes of SiO_2 are used and tested in conventional LED model. The diameters of SiO_2 in the test range from 1 μm to 20 μm. The particles' scattering properties were analyzed with Mie-scattering-based MATLAB program. SiO_2 is introduced into the yellow phosphor YAG:Ce layer to induce the scattering phenomenon within the active layer. Throughout our examination, the concentrations of SiO_2 and YAG:Ce phosphor remain constant at 5 wt.% and 10 wt.%, respectively. Our findings reveal backward scattering with 1-20 μm SiO_2 particle sizes. The backward scattering angles also change with each size. When varying the sizes of SiO_2 spheres, reduction in CCT deviation and improvements in the flux output and color rendering performance are noticed. The synthesis of SiO_2 microparticles with tunable sizes is outlined in Section 2. Section 3 provides an analysis of SiO_2 scattering and its effects on LED lighting output. Finally, Section 4 offers a conclusive summary of our examination results and suggests potential avenues for future research based on the insights gleaned from this study. The test results show that SiO_2 with larger sizes can be used for improving white LED and needs further investigations to optimize their utilization in production.

2. EXPERIMENTAL SECTION

2.1 Synthesizing Procedure

The Stober method was used to synthesize SiO_2 microspheres. Essential raw material and reaction agents include tetraethyl orthosilicate (TEOS), 3-aminopropyltriethoxysilane glutaraldehyde, polyethylene glycol diacrylate, 2-hydroxy-2-methylpropi ophenone, ethyl alcohol, and ammonia. All materials were purchased from Sigma-Aldrich. The particle sizes of SiO_2 can be adjusted by varying the concentration ratio of water, TEOS, and ethyl alcohol (Gu et al., 2021). TEOS (10 mL) and ethyl alcohol (170 mL) were combined in a beaker and stirred for 5 minutes under 60°C to achieve a uniformly mixed S1 solution, which was cleaned with water and ethanol to pH of 7, then was dried under 80°C. Subsequently, ammonia and deionized water were blended in another beaker and stirred for 5 minutes to produce a uniformly mixed S2 solution. The S2 solution was then introduced into the S1 solution and underwent a 24-hour stirring process at a consistent temperature of 20°C, with humidity levels maintained within 20-22%. Following this, the mixture underwent successive centrifugation cycles and rinses with anhydrous ethyl alcohol, culminating in the acquisition of SiO_2 powders subsequent to thermal processing under 500°C within two hours (Loan and Anh, 2020d).

2.2 LED Construction and Proficiency Assessment

Commercial YAG:Ce, compound phosphor samples altered using SiO_2 as well as blue InGaN chip units at roughly 460 nm were employed for constructing a WLED apparatus. The phosphor samples were extensively blended using epoxy sap with weight proportions for YAG:Ce and sap being roughly between 1:10 and 2:10 (Loan and Anh, 2020a). The acquired phosphor-sap compounds were daubed upon the exterior of chip units then hardened via firing under 120°C within twenty minutes inside one oven. The photoelectrical attributes for the constructed apparatus were examined via one self-temperatured LED optoelectrical assessor HAAS-2000 from Everfine (Cong and Anh, 2025). Figure 1 exhibits the characterization data of SiO_2, with Figure 1 showing the WLED apparatus.

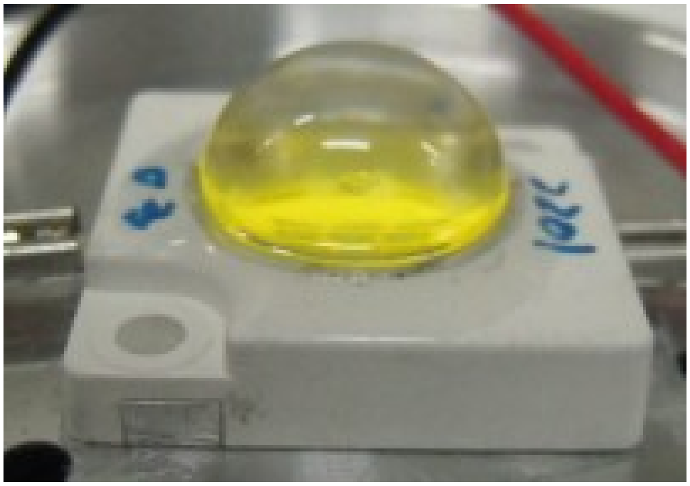

Figure 1. The WLED Model Used in This Study

2.3 Computation and Simulation

After achieving the SiO_2 microparticles with favorable spherical shape, Mie-scattering theory was applied to carried out the scattering measurements and simulation with MATLAB computing program and LightTools software (Babilon et al., 2021; Yu et al., 2021; Zhuang et al., 2021; Liu et al., 2021). The computation of SiO_2 scattering performance can be expressed as the following framework. The primary scattering measurements used for simulation include the scattering coefficient $\mu_s(\lambda)$, the anisotropy factor $g(\lambda)$:

$$\mu_s(\lambda) = \int N(r)\, C_s(\lambda, r)\, dr \qquad (1)$$

$$g(\lambda) = 2\pi \iint_{-1}^{1} p(\theta, \lambda, r)\, f(r) \cos(\theta)\, d\cos(\theta)\, dr \qquad (2)$$

where $N(r)$ indicates the distribution density of diffusional particles (mm^3), the scattering cross sections are shown by C_{sca} (mm^2) which is calculated using Equation (3), $p(\theta,\lambda,r)$

expresses the phase function which can be computed using Equation (4). θ shows the scattering angle (°C), and $f(r)$ shows the diffuser's size distribution function in the phosphor film. Additionally, λ means the light wavelength (nm), and r is the radius of scattering particle (μm).

$$C_s = \frac{2\pi}{k^2} \sum_{n=0}^{\infty} (2n-1) \left(|a_n|^2 + |b_n|^2 \right) \tag{3}$$

$$p(\theta, \lambda, r) = \frac{4\pi\, \beta(\theta, \lambda, r)}{k^2\, C_s(\lambda, r)} \tag{4}$$

in which $k = \frac{2\pi}{\lambda}$, $\beta(\theta, \lambda, r)$, $S_1(\theta)$ and $S_2(\theta)$ indicate the angular scattering amplitudes whose computations can be shown as:

$$\beta(\theta, \lambda, r) = \frac{|S_1(\theta)|^2 + |S_2(\theta)|^2}{2} \tag{5}$$

$$S_1(\theta) = \sum_{n=1}^{\infty} \frac{2n+1}{n(n+1)} \left[a_n(x, m)\, \pi_n(\cos\theta) + b_n(x, m)\, \tau_n(\cos\theta) \right] \tag{6}$$

$$S_2(\theta) = \sum_{n=1}^{\infty} \frac{2n+1}{n(n+1)} \left[a_n(x, m)\, \tau_n(\cos\theta) + b_n(x, m)\, \pi_n(\cos\theta) \right] \tag{7}$$

where a_n is the coefficient of expansion with even symmetry, b_n is the coefficient of expansion with odd symmetry, $\pi_n(\cos\theta)$ and $\tau_n(\cos\theta)$ denote the angular-dependent functions, and m shows the refractive index. The computations for the relative refractive indices of the silicone diffusor (m_{dif}) and phosphor (m_{phos}) can then be described as $m_{\text{dif}} = \frac{n_{\text{dif}}}{n_{\text{sil}}}$ and $m_{\text{phos}} = \frac{n_{\text{phos}}}{n_{\text{sil}}}$. The denseness was subject to overestimation as the sampling units underwent saturation via key granule suspension for rectifying the contrariety for the unit's refractivity index. Regarding an earlier study, the denseness for huge granules at maximumly 900 nm was assessed with the nanoscopic cavities within the granules uncovered (Bogush et al., 1988). Regardless, there is a lack of findings concerning the diametric reliance for granule denseness. Said denseness may result from the presumption that is challenging to validate on total C_{18}-series pervading on hydrophobizing process for granules. Regarding said presumption, several researchers conducted the last computations for the denseness outcomes. From another study, the denseness underwent alteration solely in the case of dual granule magnitudes (Samarov et al., 2006). In the case of granules at 315 nm, the denseness closely approached model approximation at 1.18 g cm^{-3}, while in the case of 1000 nm granules, the denseness was subject to underestimation at 1.07 g cm^{-3}.

WLED apparatuses would be designed in the form of a means between scattering, absorptivity as well as discharge influenced via one blue pump. CRI as well as CQS applied to phosphor-transmuted WLED would be preliminary factors for a radiative transfer (RT) matter. Initially, it is necessary to resolve the spectrum RT comprising wavelength-reliant Mie scattering, absorptivity as well as phosphor re-discharge for acquiring discharged SPD, then applied this SPD to color rendition parameters such as CRI as well as CQS. Alterations for spectrum absorptivity coefficient, spectrum scattering coefficient (Mie scattering), phase function, quantum yield, re-absorptivity as well as geometric data will link RT with SPD contortions responsible for CRI as well as CQS alterations. The regulating expression for radiative transfer model would be an RT expression regarding spectrum radiation $L_\lambda\ (r, s)$ (Hadi et al., 2025):

$$\hat{s} \cdot \nabla L_\lambda = -\left(\mu_a(\lambda) + \mu_s(\lambda)\right) L_\lambda + \mu_s(\lambda) \int_{4\pi} \rho(\hat{s}', \hat{s}, \lambda)\, L_\lambda(\hat{s}')\, d\Omega' + S_\lambda \tag{8}$$

where $\mu_a(\lambda)$ signifies the spectrum absorptivity coefficient (comprising latticework and phosphor re-discharge), $\mu_s(\lambda)$ signifies the spectrum scattering coefficient (Mie scattering within phosphors), $\rho(\theta, \lambda)$ signifies the scattering phase function (Mie), and S_λ signifies the source, meaning LED blue discharge as well as phosphor re-discharge. The phosphor re-discharge source under location r as well as wavelength λ is expressed via:

$$S_\lambda^{\text{ph}}(r, \hat{s}) = \eta(r) \int_{\lambda_p} \Phi_{\text{abs}}(r, \lambda_p)\, P_{\text{em}}(\lambda_p \rightarrow \lambda)\, \frac{1}{4\pi}\, d\lambda_p \tag{9}$$

where $\Phi_{\text{abs}}(r, \lambda_p)$ signifies localized absorbed blue radioactive energy denseness under exciting wavelength λ_p. η signifies phosphor intrinsic quantum proficiency (QP). $P_{\text{em}}(\lambda_p \rightarrow \lambda)$ signifies determinant discharge spectrum, typically estimated regardless of exciting process in the case of various phosphor samples, comprising Stokes shift. Re-discharge would be typically estimated in the form of isotropy but may see alteration when required.

Monte-Carlo ray tracing is the industrial standard applied to phosphor-transmuted WLED apparatuses as it can deploy various photonic clusters upon the blue pump spectrum and track re-discharged photonic granules in a fixed way, where said granules are subject to re-absorptivity once more. In the case of absorptivity via phosphors, η has a chance to discharge re-discharged photonic granules generated by $P_{\text{em}}(\lambda)$. Resolving RT, typically through Monte-Carlo ray tracing or dispersion estimation, yields an expression comprising spectrum slope caused by scattering, red penalty via re-absorptivity, blue penalty via rear-reflection, as well as angular spectrum variance:

$$\Phi_\lambda^{\text{out}} = \int_{\text{exit}} L_\lambda(\hat{s})\, \cos\theta\, d\Omega\, dA \tag{10}$$

An expression for determining CCT via the discharged SPD is shown as:

$$X = \int \Phi_{\lambda}^{\text{out}} \bar{x}(\lambda)\, d\lambda, \quad Y = \int \Phi_{\lambda}^{\text{out}} \bar{y}(\lambda)\, d\lambda, \quad Z = \int \Phi_{\lambda}^{\text{out}} \bar{z}(\lambda)\, d\lambda \qquad (11)$$

2.4 Tools and Characterization

When it comes to characterizing the constitutions, formations as well as forms for the acquired samples, multiple means were utilized. The phase clarity was assessed via Xray diffractivity (XRD) utilizing one Bruker D8 Advance powder diffractometric apparatus with Cu-Kα radioactivity across the 2θ span between 10° and 80o under room temperature under a running voltage reaching 45 kilovolts as well as an anodic current reaching 30 milliamperes. Fourier-transform infrared (FTIR) spectra were acquired via one Nicolet 6700 spectrometric apparatus from Thermo Scientific accompanied by one attenuated total reflectivity (ATR) accessory. The ATR-FTIR spectrum resolution reached 4 cm^{-1} while 128 interferogram visuals were the median for each spectrum. Form as well as power dispersal Xray spectroscopic (EDS) assessments were conducted upon one Hitachi S4800 scanning electronic microscopic apparatus (SEM) accompanied by one power dispersal Xray spectroscopic apparatus (EDX) as well as one FEI Tecnai G^2 F20 S-WTINE transference electronic microscopic apparatus (TEM) functioning under 200 kilovolts. TEM samples were made via desiccating one dripping of thinned ethanol dispersal for the sample upon the exterior for one carbon-daubed copper lattice. The SPD for the sum radiance flux was assessed via utilizing one LMS-100 incorporating globe from Labsphere Inc. linked with one USB2000 CCD tracker from Optics Inc. accompanied by one optical filament. Figures 2 (a)-(d) depict SEM, TEM, XRD, and FTIR spectrum respectively.

3. RESULTS AND DISCUSSION

3.1 SEM

The magnitudes as well as forms for the acquired sampling units were assessed via SEM and TEM, with visuals shown by Figures 2(a) and 2(b). YAG:Ce exhibited desirable dispersal, an almost globular form as well as a median magnitude reaching roughly 1 μm. The globular form typically prefers greater drifting ability, bundling denseness along with smaller illumination dispersion, facilitating utilization in WLED. Under a deeper look, the exteriors for the microsphere units proved coarse, bumpy and exhibited auto-assemblage via far tinier nanoscopic units. Said mechanism suggests the polycrystal nature for the microspheres, validated via specific zone electronic diffractivity. A number of subtly allocated diffractivity locations manifested, instead of symmetry-set locations or hoops.

3.2 TEM

TEM visual shown by Figure 2(b) and acquired upon the rim of a singular microsphere exhibits noticeable latticework rims for cuboid YAG:Ce, suggesting significant crystallizing level. The inter-plane gaps of roughly 0.27 as well as 0.17 nm would respectively match the d-gaps for the (420) as well as (444) crystal surfaces. The exterior alterations were conducted for yielding a combination of SiO_2 and YAG:Ce. A noticeable SiO_2 outward sheet manifested because of the smaller contrariety relative to the intrinsic YAG:Ce nucleus. The breadth reached roughly 80 nm posterior to a single daubing sequence then surged to roughly 150 nm posterior to dual daubing sequences. Based on the elementary assessment via EDS, the doping Ce dosage reached roughly 3% while the Y(Ce)/Al granular proportion reached roughly 0.58, matching nominal outcomes well.

3.3 XRD

The phase constitutions as well as the crystalline nature for the acquired sampling units underwent assessment via XRD. In Figure 2(c), the XRD profile for said units exhibited the generation of crystal yields. There is no sight of clear distinctive diffractivity apexes for the median phases. Every pronounced apex was thoroughly applied to the cuboid stage for YAG having ICDD no. 33-0040, suggesting a far tinier crystal magnitude. The supplementary exterior daubing for the formless SiO_2 upon YAG:Ce avoided yielding a broadband with apex under 2θ and 22° even posterior to dual daubing sequences because of its tiny quantity.

3.4 FTIR Spectrum

On the contrary, the FTIR spectra seen in Figure 2(d) exhibit the absorptivity band for Si−O−Si bindings posterior to exterior alterations, while the intenseness surged as the daubing processes were redone. There was an absence of oscillatory states. Within the small-periodicity span between 400 and 800 cm^{-1}, the pronounced absorptivity bands under roughly 6787 as well as 778 cm^{-1} showed a link to the states for Al−O as well as Y−O bindings. Furthermore, a faint and noticeable band manifested under roughly 1580 cm^{-1}, suggesting the generation for protonated key amine categories (NH^{3+}), and would be linked to the periodicity of NH^{3+} symmetrical contortion. The protonating process typically altered the oscillation for said amine towards a smaller periodicity. Said mechanism suggested that protonated ethanol covered the exteriors or interfacial planes for the sampling units via binding with metallic elements such as Y^{3+}, Ce^{3+}, or Al^{3+} because of their internal preference of amine categories. Based on observation, the exterior organic amine categories showed resistance against heat. However, they began desorbing from the sampling unit under 100°C, and total elimination was solely attained at maximumly 1000°C.

3.5 Correlation of Mie Scattering with Optical Attributes

The scattering performance of SiO_2 within the conversion phosphor layer, spanning diameters from 1 μm to 20 μm, is meticulously detailed in Figure 3. Figure 3(a) depicts scattering coefficient under angles, while Figures 3(b) and 3(c) depict scattering coefficient under a wavelength range of 300-800 nm, and 380-780 nm, respectively. Observable illumination would be optimally scattered via granules with magnitude approaching the wavelength of Mie scattering. Granules under Rayleigh

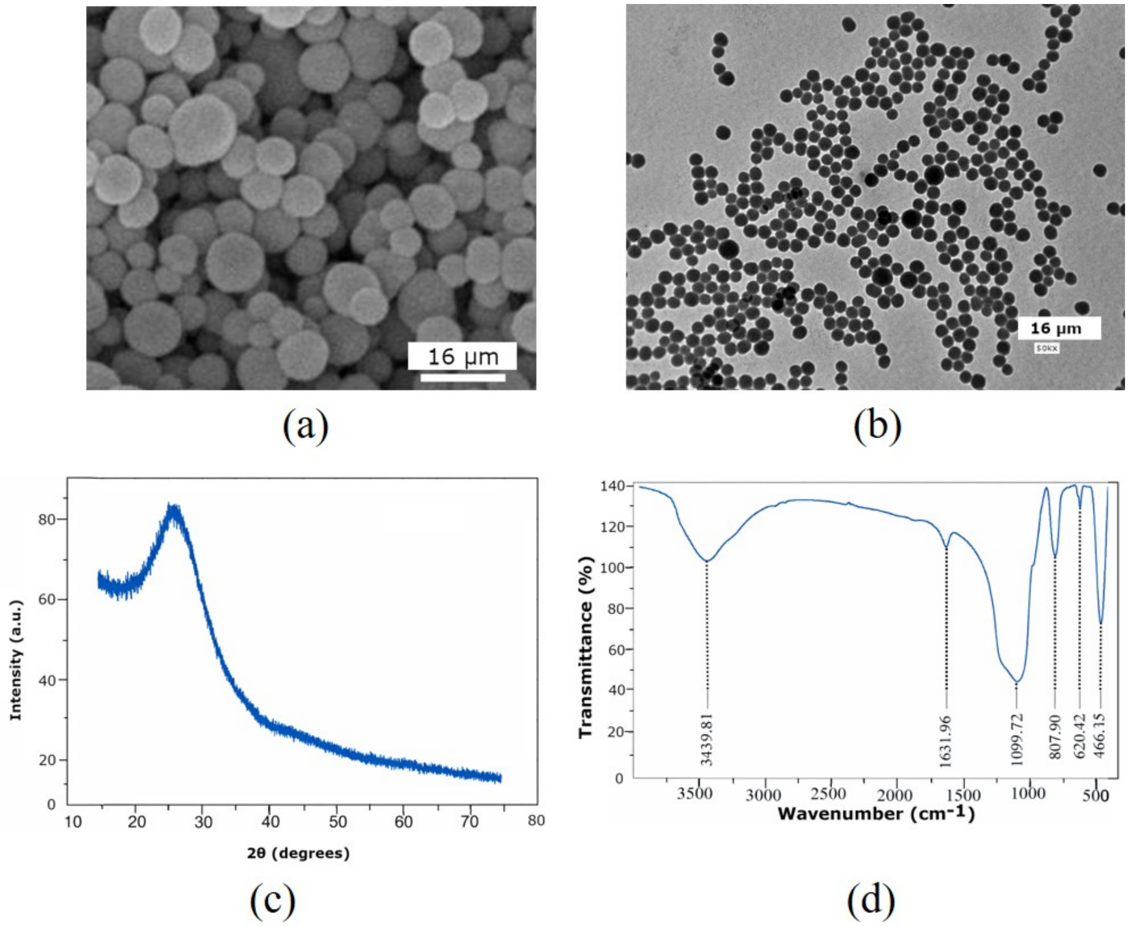

(a) (b)

(c) (d)

Figure 2. Characterization Data of SiO_2: (a) SEM, (b) TEM, (c) XRD Pattern, (d) FTIR Spectrum

setting exhibit particularly faint scattering as well as high reliance upon wavelength, while granules with small sizes in the micron range exhibit potent, wide dispersion throughout the observable light (Loan and Anh, 2020b). In LED application, there are disparate options regarding particle size. When it comes to chroma homogeneity as well as blending between volume and phosphor sheet, optimal particles range from high nanometers to roughly 1 μm. At 1 μm, desirable dispersion can be attained. Regarding exterior dispersers, bigger granules in µm would be typically employed, with products exhibiting common size spans such as between 2 and 20 μm to achieve potent dispersion in molded lens units. When the goal is uniform chroma blending within phosphor and silicone sheets, i. e. small lumen penalty and greater homogeneity, low-micron granules from 0.2 to 1 μm are preferred for maximizing Mie dispersion throughout observable illumination whilst maintaining desirable transference. When the goal is particularly potent dispersion upon the package exterior, granules with a greater micron range from 3 to 10 μm yield wider-angle dispersion while reducing fore transference. Across all particle sizes, an effective forward scattering angle of ±60° (or 60°-300°) is observed, which holds significant importance in the context of LED devices. Furthermore, a minor range of backward scattering is discernible by the scattering line within the backward hemisphere (Zhang et al., 2021; Duan et al., 2021; Wang et al., 2021). The propensity for backscattering among particles is intricately tied to their respective size distributions, showcasing notable disparities in the levels of backscattered light energy across different particle sizes. In the simulation test with the results exhibited in Figure 3, it can be seen that the intensity and shape of forward scattering do not pose notable changes, but those of back-scattering do. The back-scattering of 17 μm presents the same shape to that of the 16 μm, yet the angle seems to be narrower and the intensity is less than those of 16 μm. The backscattering line of 18 μm is significantly different from that of the others. It demonstrates the backscattering events happen mostly within 150-210 degrees angular range. The backscattering of 19 μm and 20 μm is quite similar, but the back-scatter intensity in the case of 20 μm is smaller than one in the 19-μm case.

Such differences in backward scattering events have different effects on the lumen output of the LED, as illustrated in Figure 4. When illumination enters Mie scattering setting, employable lumen generated by phosphor-transmuted WLED

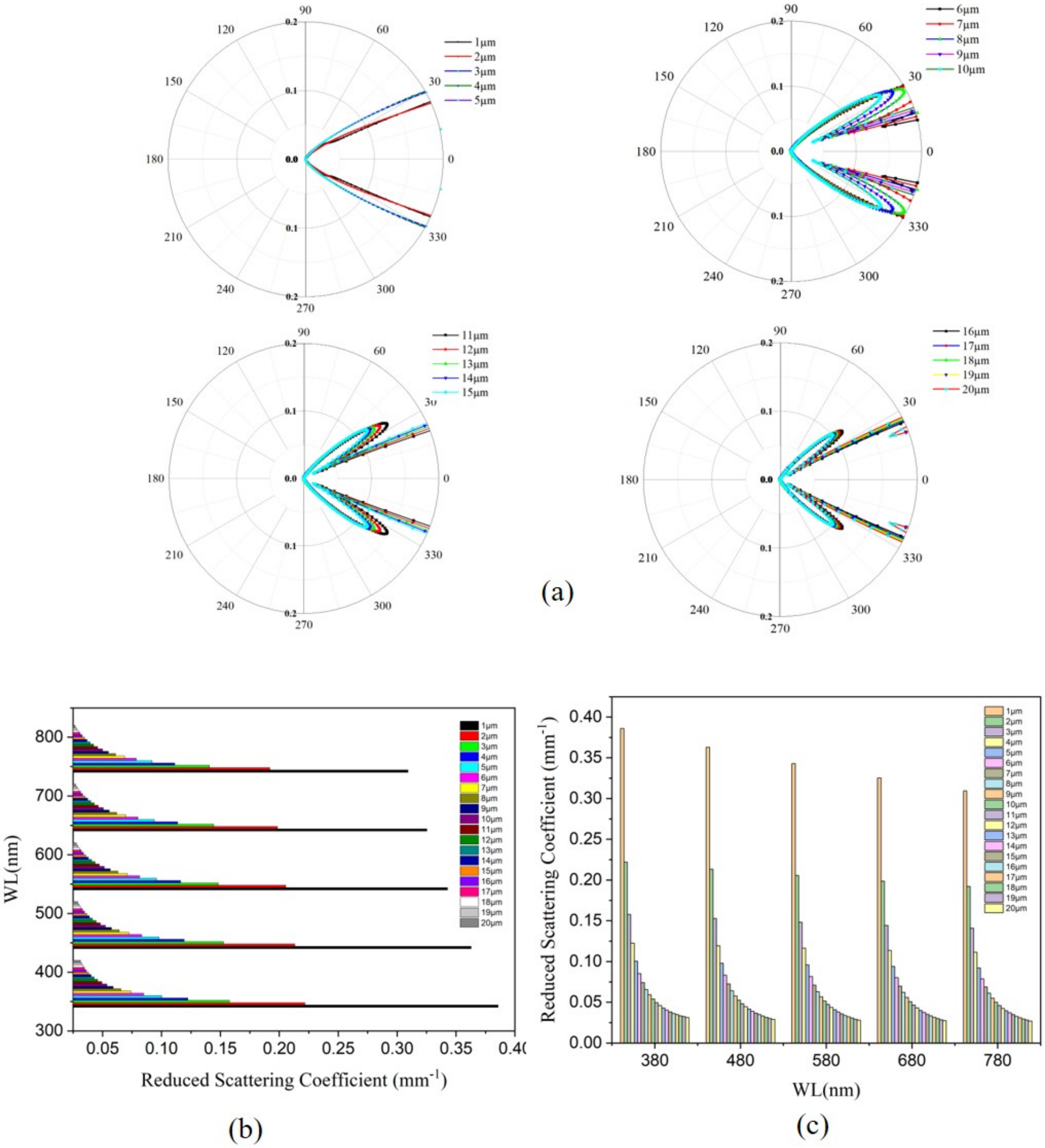

Figure 3. Scattering Performance with Different SiO_2 Diameters: (a) Scattering Coefficient Under Angles, (b) Scattering Coefficient Under a Wavelength Range of 300-800 nm, (c) Scattering Coefficient Under a Wavelength Range of 380-780 nm

is typically lessened as Mie scattering causes photonic granules to assume extended pathways, meaning greater absorptivity as well as re-absorptivity, leading a portion of illumination unto absorbing portions in the WLED setting (Loan and Anh, 2020e). Mediumly potent Mie scattering assists in chroma blending as well as angle consistency with a lumen penalty. Specifically, more extensive optical pathways cause greater absorptivity. Scattering results in undulating movement of photonic granules within phosphors and as such, said granules travel across additional substances and tend to be subject to absorptivity via phosphors prior to transmutation or via metallic remnants, Mie scattering would not be entirely forward as a portion would be led back to the LED chip in which it is subject to absorptivity rather than extrication. Scattering potency relies upon wavelength since blue and yellow/red would be dispersed disparately and as such, the spectrum including CCT, CRI, CQS as well as lumen may be altered. Regarding angular reallocation, scattering has a high chance of increasing Lambertian attribute in discharge, which benefits homogeneity. However, this would not generate lumen, but rather reallocate it. All absorptivity manifesting throughout the reallocation would be a lumen penalty. It is possible for photonic granules transmuted via phosphors to undergo re-absorptivity via adjacent phosphor granules when scattering holds said granules within the

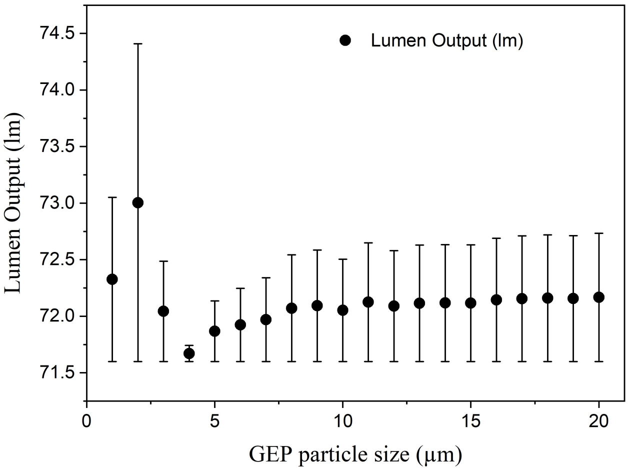

Figure 4. The LED's Lumen Output as a Function of Varying SiO_2 Radius

phosphor sheet, lowering extrinsic lumen. As such, there are trade-offs in practical application. Bigger and optimal granule magnitude shift scattering unto a greater forward setting or lessen scattering for each granule, boosting extrication.

Lesser granule load or narrower phosphor sheets, leading to less scattering activities while possibly lessening transmutation proficiency, which is a compromise between chroma/energy and lumen. It is possible to modify fore dispersers or optical sheets by altering scattering phase function (potent fore anisotropy) for leading illumination to shift extrinsically. Extricating components with textures such as lenses and exterior attributes transmuted captured states to extricating pathways, limiting scattering penalties. In short, Mie scattering proves to be a mixed blessing as it augments chroma blending as well as angle consistency while lessening lumen due to heightened absorptivity as well as rear-reflection. The lumen cost relies upon granule magnitude, scattering coefficient, absorptivity coefficient, anisotropy as well as sheet setting. The backward scattering is unfavorable to the lumen intensity of the LED, though it reported that larger particles size often gives higher transmission intensity as the incident light is easier to pass through the particle and get extracted. Generally, the lumen intensity increases with enlarging SiO_2 diameter, but the increase is insignificant between each size. According to Figure 4, the highest lumen is with 20 μm while the lowest is with 16 μm of SiO_2 sizes.

Based on the SPD for YAG:Ce subject to LED excitation at 465 nm, the broad discharge band showed an apex under 530 nm, generated by the shift between 5d and 4f in Ce. The intensity proportion for exciting as well as discharge illumination showed variance alongside the sampling unit's breadth. The photoluminescent intenseness for the unit with a breadth of 0.632 mm surpassed the propagated exciting illumination under 465 nm.

In terms of color reproduction performance of the LED, the color rendering index CRI and color quality scale CQS are assessed, as shown in Figure 5. Figures 5(a) and 5(b) depict color rendering index (CRI) and color quality scale (CQS), respectively. Mie scattering typically has an unfavorable influence on CRI as well as CQS. While it does not generate or eliminate spectrum apexes, it reallocates, re-absorb as well as contorting the illumination spectrum within one phosphor sheet, thus altering the discharged spectrum as well as chroma saturation to lessen chroma rendition outcomes. As stated above, Mie scattering potency shows variance under wavelength. Blue, green as well as red elements shows disparate scattering and as such, the extricated spectrum may be altered, typically lessening red yield compared to blue as well as yellow. Scattering boosts photonic pathway span and as such, transmuted photonic granules, particularly red as well as near IR, would have a greater chance of being subject re-absorptivity instead of escaping, irregularly lessening red element and subsequently degrading CRI as well as CQS.

Various scatterings as well as re-discharge have a high chance of widening as well as smoothening discharge bands, lessening spectrum contrariety or saturation, meaning that CQS would see a greater penalty compared to CRI under an identical spectrum variance. Scattering induces spectral alteration under discharge angle. CRI may seem decent under an angle while might be perceived as bad under other angles. CQS, the observed color quality, may see a penalty as entity chromas show variance under observing angles. Medium scattering can augment blue phosphor blending, lessening chroma hoops, and augmented assessed factors when the original model shows undesirable blending. Regardless, excessive scattering will generate spectrum penalties. CQS comprises factors such as saturation, chromatic sustainment as well as viewer choice besides uniformity throughout additional sampling chromas. As scattering typically lessens saturation as well as red consistency, CQS may decline quicker with a bigger quantity compared to CRI under an identical spectrum alteration caused by scattering. It is essential to consider viable designing for alleviating undesirable influences on color rendition. It is possible to boost particle size or augment size allocation, lessening reliance of scattering on wavelength or shifting towards additional fore scattering. Optical sheets, fore anisotropy dispersers as well as extrication formations can maintain extrication under concurrent illumination blending. It is also possible to regulate phosphor sheet breadth as well as load for balancing transmutation and scattering. The SPD computation can be applied to determine CRI as well as CQS. In the case of CRI, it is necessary to calculate testing chroma sample reflectivity shone via testing as well as referential SPDs, transmute into a homogenous chroma space, determine Euclidean chroma disparities as well as amalgam. Usually, CRI Ra would utilize eight sampling units and supplementary peculiar index such as R9 would be determined individually.

In the case of CQS, it utilizes a bigger series of testing chromas, a newer coloring space, determines perceived chroma ranges, utilizes homogeneity, saturation as well as preferences

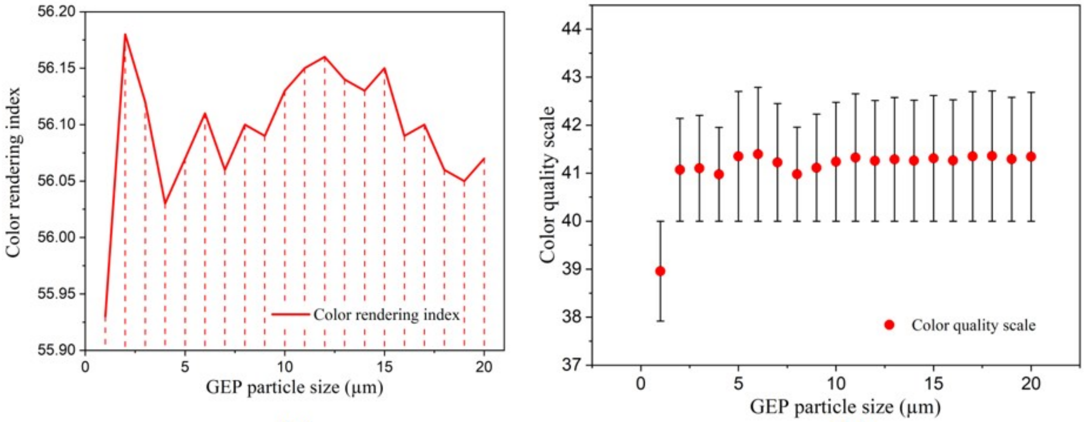

(a)

(b)

Figure 5. The Rendering Performances of LED White Illumination as a Function of Varying SiO_2 Radius: (a) Color Rendering Index and (b) Color Quality Scale

throughout sampling units for generating a singular CQS result and CQS can yields a penalty for saturation as well as preference. RT factors can significantly influence CRI as well as CQS. Absorptivity or re-absorptivity under high wavelengths under roughly from 600 to 650 nm lessens R9 and substantially degrades CRI as well as CQS. Spectrum form for phosphor discharge as well as QP can cause small red QP or small red discharge portion, leading to smaller CRI as well as CQS.

Significant scattering coefficient as well as anisotropic factor boosts angular dispersion as well as re-absorptivity, causing spectrum smoothening as well as desaturating process. As such, CQS is subject to greater deterioration compared to CRI. The wavelength reliance of anisotropic factor results in the angle reliance in CCT as well as CRI. Rear-reflection unto lossy exteriors eliminates spectrum elements in an ununiform way. The phosphor particle size as well as index contrariety will decide Mie cross-sections as well as phase functions, hence the wavelength reliance of scattering coefficient as well as anisotropic factor. The CRI and CQS display a certain trend, increasing as the SiO_2 particle sizes reach a certain value and start declining afterwards. In Figure 5a, the CRI reaches its highest value with SiO_2 particle size of 17 μm while in the case of CQS, 18 μm results in the greatest value. The lowest level of CRI and CQS is all noted with 19 μm of SiO_2 diameter. Though the decrease or increase is not too significant among different SiO_2 sizes, it indicates that large SiO_2 spheres can induce the color rendition of the LED (Evéquoz et al., 2021; Wang et al., 2021; Chen et al., 2021).

The angular color uniformity in connection with the radius of SiO_2 is illustrated in Figure 6. Figures 6(a) and 6(b) depict angular correlated color temperature (CCT) and delta-CCT (D-CCT), respectively. Mie scattering typically generates variance in angular CCT in a notable degree. As scattering relies upon wavelength and shows direction bias, the SPD seen by observers is altered alongside angles. As CCT is based on SPD, CCT proves to be reliant upon angles, Mie scattering proficiency relies upon the particle size as well as wavelength. Blue, green as well as red spectrum elements will scatter disparately and as such, the balancing among blue and yellow/red photonic granules shows variance under pathways. The phase function or its asymmetry factor decides whether illumination prefers fore movement or gets led to big angles. When smaller wavelength levels possess a disparate asymmetry factor compared to bigger counterparts, the angular SPD slopes alongside angles. For various WLED apparatuses, there are key blue discharge as well as transmuted discharge generated via allocated phosphor granules. Said means possess disparate angular discharge posterior to scattering and as such, the relative influence between blue and transmuted illumination is altered alongside angles. Various scatterings will boost pathway span as well as chance of re-absorptivity, which is typically reliant on wavelength. Said mechanism specifically eliminates or re-allocates particular bands to a greater degree under certain angles compared to other counterparts, altering CCT alongside angles. Rear-reflected illumination might be subject to absorptivity while the angular profile for such penalties would not be homogenous. Subsequently, certain observing angles perceive additional proportion of the penalty, altering observed CCT.

Regarding measuring geometry, the sum flux of incorporating globe yields a singular median SPD or CCT. On as well as off-pivot spectroradiometry measuring tasks can uncover the angular CCT variance that can be observed within an apparatus. When it comes to angular shift from warm to chill or chill to warm, general pathway does not apply. Said shift relies upon the phosphor sheet, particle size as well as sheet breadth. Potent fore scattering lessens angular SPD alteration, meaning smaller angle movement, while greater isotropy scattering typically boosts angular CCT variance. Approaches for lessening angular CCT variance include boosting fore anisotropic factor by picking particle sizes as well as refraction index contrariety shown in

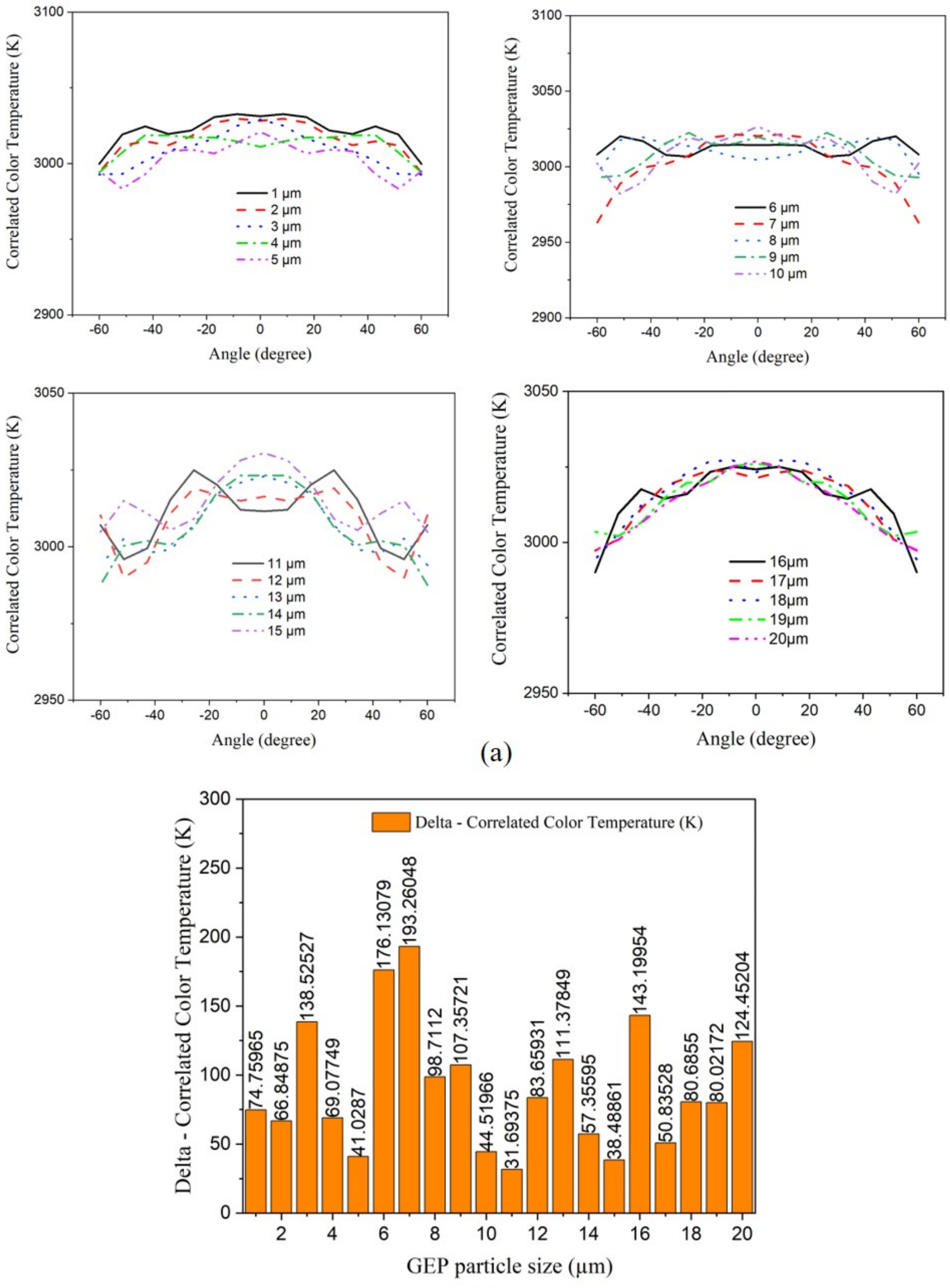

(a)

(b)

Figure 6. The Color Temperature Divergence of the LED Illumination as a Function of Varying SiO_2 Radius: (a) Angular Correlated Color Temperature (CCT) and (b) Delta-CCT (D-CCT)

Figure 7 favoring fore dispersion. It is possible to employ bigger phosphor granules or optimal size allocation for lessening high wavelength reliance. Another approach involves lessening phosphor sheet thickness or adjusting granule load at the

Table 1. Result Comparison of Scattering Coefficients Influenced by Particle Sizes of Scattering Materials

Scattering Materials	Scattering Coefficients (mm^{-1})	Reduced Ccattering Coefficients (mm^{-1})	References
SiO_2	0.593	0.037	This work
KBr	42.5	13.5	(Anh et al., 2025)
MgO	3.54	0.059	(Loan and Chen, 2025)

Table 2. Comparative Table of This Research Results with Reported Research

Scattering materials	CCT (K)	D-CCT (K)	CRI	CQS	Lumen (lm)	References
SiO_2	3000	50.6	56.1	41.36	72.16	This work
KBr	3000	35.4	56.2	42.4	73.7	(Anh et al., 2025)
MgO	4000	53.6	58.2	64.2	131.1	(Loan and Chen, 2025)

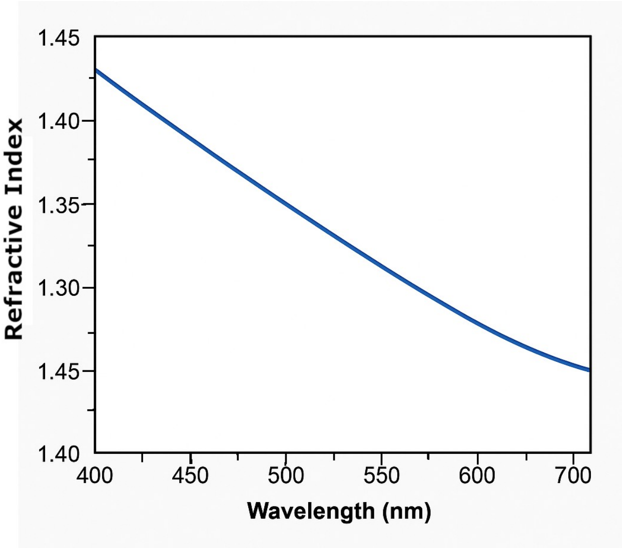

Figure 7. Refractive Index of SiO_2

cost of transmutation proficiency against angle homogeneity. Introducing optical forming via supporting optic components, lenses or disperser sheets made for blending angles can sustain spectrum, meaning narrow modified dispersers which blend by direction while avoiding boosting re-absorptivity. Two parameters, angular-CCT range (Figure 6a) and D-CCT (Figure 6b), are taken into consideration. The fluctuation is noticeable in response to the varying SiO_2 sizes. The angular-CCT intensity at the center (0°) is likely to be flattened or decrease when SiO_2 with diameters larger than 17 μm. This implies that the blue light is redirected by the SiO_2 and dispersed across larger angles, indicating that the color divergence among different angles could be reduced to enhance the color uniformity. Such an assumption can be validated with the data illustrated in Figure 6b. The lowest is D-CCT is observed with a SiO_2 size of 17 μm while the highest one is with 16 μm. Such an outcome support to achieve the goal of the study is to test whether it is possible to obtain improvements in color distribution uniformity with larger particle sizes of SiO_2 (That et al., 2020).

The relationship between the spectral power and different ranges of SiO_2 particle size is depicted in Figure 8 with Figure 8(a) showing particle sizes from 1 to 10 μm, while Figure 8(b) shows particle sizes from 11 to 20 μm. As can be seen in Figure 8(a) with a particle size range of 1 to 10 μm, the spectral power shows two pronounced peaks across a wavelength range of 400 to 800 nm. In its first peak, the spectral power is at its lowest with no changes from a wavelength range of 400 to 420 nm. However, as the wavelength reaches nearly 450 nm, the spectral power begins to show a significant and consistent surge under most particle sizes in this range, before reaching the peak at roughly 450 nm. As the wavelength exceeds 450 nm, the spectral power shows an equally significant decline down to 480 nm, which is almost as low as its counterpart at 420 nm. In the second peak, the spectral power follows an identical changing pattern at all particle sizes, initially starting at a low value before surging to the highest outcome at a median wavelength of roughly 590 nm, then plummeting beyond this point. Figure 8(b) features spectral power under a particle size range of 11 to 20 wt.% within the same wavelength range and dual apexes from Figure 8(a). Compared to the particle size range of 1 to 10 wt.%, the spectral power in the range of 11 to 20 wt.% shows noticeably more fluctuations and less consistent surges, but its changing pattern remains partially the same.

Mie scattering generated by SiO_2 granules can reshape the SPD in WLEDs via extending photonic pathways to yield greater absorptivity as well as transmutation, reallocating angles reliant on wavelength to alter balance of blue, red, and yellow elements, along with boosting re-absorptivity or rear penalty to increase the chance of eliminating the red tail. Said mechanism leads to a decline in blue apex, a median-band ridge via additional transmutation, as well as an irregular penalty for deep red, accompanied by SPD alterations reliant on angles. More extensive optical pathways lead to greater absorptivity or re-discharge. Scattering allows blue pumping photonic granules to traverse at a greater distance via the phosphor to be

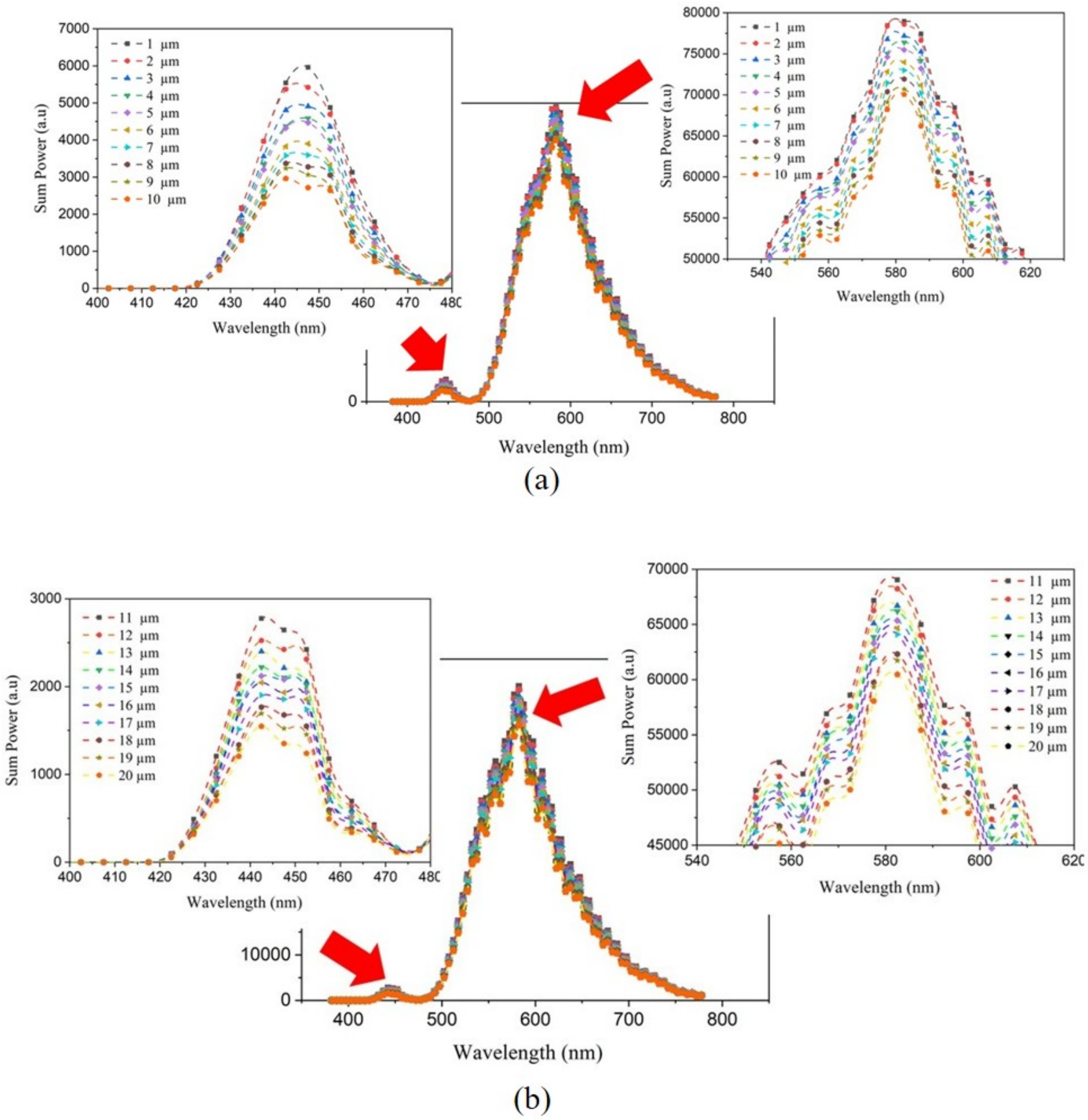

(a)

(b)

Figure 8. Spectral Power Under Different Ranges of SiO_2 Particle Size: (a) Particle Sizes from 1 to 10 μm, (b) Particle Sizes from 11 to 20 μm

subject to additional absorptivity as well as transmutation. Said mechanism has a high chance of lessening on-pivot blue energy and boost transmuted bands for warmer points, however, supplemental absorptivity may become nonradioactive, lessening total spectrum power. Mie cross-sections as well as the asymmetric factor change alongside wavelength as well as particle size. Since blue, green as well as red elements would be dispersed disparately, the angular SPD is altered alongside observing CCT angle while the incorporated SPD may slope.

Various scatterings result in the re-absorptivity for transmuted photonic granules. Transmuted yellow/red photonic granules inhabit within the phosphor sheet for a greater period and has a higher chance of being subject to re-absorptivity and potentially eliminated. Red would be typically most affected when R9 declines. Regarding angular reallocation between blending and penalty, scattering can augment space or chroma blending with less hoops but will suffer from spectrum penalties when absorptivity or rear penalty manifests throughout the additional scattering activities. The result comparison of optical attributes between SiO_2 and its counterparts Kbr and MgO can be seen in Tables 1 and 2, showing its ability to yield color rendition comparable to said counterparts.

4. CONCLUSIONS

In this study, the utilization of larger SiO_2 particles within a conventional LED model, ranging in diameter from 0 μm to

20 μm, is demonstrated employing the Stober method, Mie-scattering-based MATLAB program, and LightTools software to simulate the optical attributes of a phosphor-transmuted WLED apparatus. Integration of SiO_2 into the yellow phosphor YAG:Ce layer facilitated the inducement of scattering phenomena within the active layer. Through our examination, the concentrations of SiO_2 and YAG:Ce phosphor were meticulously maintained at 5 and 10 wt.%, respectively, ensuring consistency across our experimental parameters. Notably, a discernible reduction in angular color temperature deviation and concurrent enhancements in both flux output and color rendering performance are observed as we varied the sizes of SiO_2 spheres. These results emphasize the potential efficacy of larger SiO_2 particles in augmenting the performance of white LEDs. However, despite these promising outcomes, there are rooms for further investigations to optimize the utilization of larger SiO_2 particles in LED production processes by delving deeper into the intricacies of particle size variations and their effects on scattering behaviors of radiating components in different LED types.

5. ACKNOWLEDGMENT

The authors wish to express their gratitude to the Posts and Telecommunications Institute of Technology, Vietnam, for financial support for this research.

REFERENCES

Anh, N. D. Q., N. T. P. Loan, P. V. De, and H. Y. Lee (2025). Potassium Bromide Scattering Simulation for Improving Phosphor-Converting White LED Performance. *Optoelectronics and Advanced Materials-Rapid Communications*, **19**; 378–383

Babilon, S., J. Klabes, P. Myland, and T. Q. Khanh (2021). Memory Colors and the Assessment of Color Quality in Lighting Applications. *Optics Express*, **29**(18); 28968

Bogush, G., M. Tracy, and C. Zukoski (1988). Preparation of Monodisperse Silica Particles: Control of Size and Mass Fraction. *Journal of Non-Crystalline Solids*, **104**(1); 95–106

Bugoffa, S. G. and M. R. Chatterjee (2021). Electromagnetic and Imaging Properties of Chiral Dispersive Spherical Interfaces under Bimodal Propagation Using ABCD Matrices. *Applied Optics*, **60**(25); 7804

Buzzelli, M. and I. Erba (2021). On the Evaluation of Temporal and Spatial Stability of Color Constancy Algorithms. *Journal of the Optical Society of America A*, **38**(9); 1349

Chen, Z., J. Su, X. Zeng, X. Huang, Y. Li, and C. Huang (2021). Electron Angular Correlation in Nonsequential Double Ionization of Molecules by Counter-Rotating Two-Color Circularly Polarized Fields. *Optics Express*, **29**(18); 29576

Cong, P. H. and N. D. Q. Anh (2025). Augmenting Chroma Performance for WLED Employing $SR_8ZNSC(PO_4)_7$:Eu^{2+}@ALAS as a Scattering-Enhancing Substance. *Science & Technology Indonesia*, **10**(2); 467–472

Dang, H. P., P. T. That, and N. D. Q. Anh (2021). Utilizing $CaCO_3$, CaF_2, SiO_2, and TiO_2 Phosphors as Approaches to the Improved Color Uniformity and Lumen Efficacy of WLEDs. *TELKOMNIKA (Telecommunication Computing Electronics and Control)*, **19**(2); 623

Duan, D., R. Zhu, and Y. Xia (2021). Color Night Vision Ghost Imaging Based on a Wavelet Transform. *Optics Letters*, **46**(17); 4172

Evéquoz, G., F. Truffer, and M. Geiser (2021). Maximum Possible Contrast Level for Silent Substitution: A Theoretical Model Applied to Melanopsin Stimulation. *Journal of the Optical Society of America A*, **38**(9); 1312

Gao, S., Z. Tian, P. Yu, H. Sun, H. Fan, Q. Chen, and H. Sun (2021). Deep Diamond Single-Photon Sources Prepared by a Femtosecond Laser. *Optics Letters*, **46**(17); 4386

Gu, D., C. Liang, L. Sun, H. Chen, Y. Chen, and L. Yang (2021). Optical Metasurfaces for Waveguide Couplers with Uniform Efficiencies at RGB Wavelengths. *Optics Express*, **29**(18); 29149

Hadi, D. S., H. Wafda, A. P. A. Mustari, V. Trisnawan, N. Widiawati, F. Miftasani, and D. H. Prajitno (2025). Corrosion Behavior of Modified F/M Steel with Ti and Dispersed Oxides: Y_2O_3 and ZrO_2 under High Temperature in Static Liquid Lead. *Science & Technology Indonesia*, **10**(3); 877–888

Li, X., S. Fu, J. Miao, M. Zhang, and X. Zhang (2021). Adjustable Color Response during Plasmon Resonance by Monochromatic Light Irradiation. *Optics Letters*, **46**(17); 4296

Liu, Q., M. Fu, H. Jiang, H. Ren, M. Cai, X. Zeng, and Q. Zhuge (2021). Subcarrier-Pairing Entropy Loading for Digital Subcarrier-Multiplexing Systems with Colored-SNR Distributions. *Optics Express*, **29**(18); 28852

Loan, N. T. P. and N. D. Q. Anh (2020a). The Effectiveness of $MgCeAl_{11}O_{19}$:Tb^{3+} Phosphor in Enhancing the Luminous Efficacy and Color Quality of Multi-Chip White LEDs. *International Journal of Electrical and Computer Engineering*, **10**(5); 4631

Loan, N. T. P. and N. D. Q. Anh (2020b). The Effects of ZnO Particles on the Color Homogeneity of Phosphor-Converted High-Power White LED Light Sources. *International Journal of Electrical and Computer Engineering*, **10**(5); 5155

Loan, N. T. P. and N. D. Q. Anh (2020c). $LaSiO_3Cl$:Ce^{3+},Tb^{3+} and Mg_2TiO_4:Mn^{4+} Quantum Dot Phosphors for Improving the Optical Properties of WLEDs. *International Journal of Electrical and Computer Engineering*, **10**(5); 5191

Loan, N. T. P. and N. D. Q. Anh (2020d). $Na_3Ce(PO_4)_2$:Tb^{3+} and $Na(Mg_{2-x}Mn_x)LiSi_4O_{10}F_2$:Mn Phosphors: A Suitable Selection for Enhancing Color Quality and Luminous Flux of Remote White Light-Emitting Diodes. *TELKOMNIKA (Telecommunication Computing Electronics and Control)*, **18**(4); 2095

Loan, N. T. P. and N. D. Q. Anh (2020e). Utilizing $CaCO_3$, CaF_2, SiO_2, and TiO_2 Particles to Enhance Color Homogeneity and Luminous Flux of WLEDs. *International Journal* *of Electrical and Computer Engineering*, **10**(5); 5175

Loan, N. T. P. and M. J. Chen (2025). Influences from MgO-Doped Phosphors on Optical Properties of White Light-Emitting Diodes. *Journal of Advanced Engineering and Computation*, **9**(2); 49–57

Masaoka, K. (2021). Proper Application of Chromaticity Gamut Area Metrics for Displays. *Optics Express*, **29**(18); 29107

Navarro, R., S. Baquedano, and A. I. Sánchez-Cano (2021). GRINCU Lens with Conicoid Iso-Indicial Surfaces: Application for Modeling the Crystalline Lens. *Optics Express*, **29**(20); 30998

Pi, D., J. Liu, and S. Yu (2021). Speckleless Color Dynamic Three-Dimensional Holographic Display Based on Complex Amplitude Modulation. *Applied Optics*, **60**(25); 7844

Preciado, O. U., A. Martin, E. Manzano, K. A. G. Smet, and P. Hanselaer (2021). CAM18sl Brightness Prediction for Unrelated Saturated Stimuli Including Age Effects. *Optics Express*, **29**(18); 29257

Rahman, M. A., Y. H. Kim, S. Cho, S. Y. Lee, and J. Y. Byun (2021). Realization of Structural Colors via Capped Cu-Based F–P Cavity Structure. *Optics Express*, **29**(18); 29466

Samarov, E. N., A. D. Mokrushin, V. M. Masalov, G. E. Abrosimova, and G. A. Emel'chenko (2006). Structural Modification of Synthetic Opals during Thermal Treatment. *Physics of the Solid State*, **48**(7); 1280–1283

Suchkov, N., T. Kurian, C. Schwarz, A. Leube, and S. Wahl (2021). SLM-Based Interferometer for Assessing the Polychromatic Neural Transfer Function of the Eye. *Biomedical Optics Express*, **12**(10); 6040

Sun, Y., J. Zhang, and R. Liang (2021). Color Polarization Demosaicking by a Convolutional Neural Network. *Optics Letters*, **46**(17); 4338

That, P. T., T. M. Bui, N. T. P. Loan, P. X. Le, N. D. Q. Anh, and L. Van Tho (2020). Dual-Layer Remote Phosphor Structure: A Novel Technique to Enhance the Color Quality Scale and Luminous Flux of WLEDs. *International Journal of Electrical and Computer Engineering*, **10**(4); 4015

Thi, M. H. N., T. M. Bui, and N. D. Q. Anh (2021). Aiming to the Superior of Phosphor Pattern: Influence of SiO_2 Nanoparticles on Photoluminescence Intensification of YAG:Ce. *International Journal of Electrical and Computer Engineering*, **11**(6); 4833

Wang, J., X. Wang, P. Zhang, S. Xie, S. Fu, Y. Li, and H. Han (2021). Correction of Uneven Illumination in Color Microscopic Image Based on Fully Convolutional Network. *Optics Express*, **29**(18); 28503

Yamashita, K., K. Kunitsu, T. Hattori, Y. Kuwahara, and A. Saito (2021). Demonstration of a Diffraction-Based Optical Diffuser Inspired by the Morpho Butterfly. *Optics Express*, **29**(19); 30927

Yu, B., Z. Lu, G. Liang, Y. Yuan, H. Wang, J. He, and S. Yang (2021). Luminous Efficacy Enhancement for LED Lamps Using Highly Reflective Quantum Dot-Based Photoluminescent Films. *Optics Express*, **29**(18); 29007

Zhang, C., R. Niu, P. Sha, X. Li, H. Ma, and Y. Sun (2021). Inner Helical Waveplate with Angle-Insensitive Retardation. *Optics Express*, **29**(18); 28924

Zhou, J., T. Yang, W. Ren, D. Zhang, and W. Zhang (2021). Underwater Image Restoration via Depth Map and Illumination Estimation Based on a Single Image. *Optics Express*, **29**(19); 29864

Zhuang, Z., D. Iida, M. Velazquez-Rizo, and K. Ohkawa (2021). 630-nm Red InGaN Micro-Light-Emitting Diodes ($<20\ \mu m \times 20\ \mu m$) Exceeding 1 mW/mm^2 for Full-Color Micro-Displays. *Photonics Research*, **9**(9); 1796